CHEMISTRY OF MATERIALS

pubs.acs.org/cm

Article

Geometric Frustration and Concerted Migration in the Superionic Conductor Barium Hydride

Gavin J. Irvine,* Franz Demmel, Helen Y. Playford, George Carins, Martin Owen Jones, and John T. S. Irvine*

Cite This: https://doi.org/10.1021/acs.chemmater.2c01995

Read Online

ACCESS | Metrics & More | Article Recommendations | Supporting Information

ABSTRACT: Ionic conductivity is a phenomenon of great interest, not least because of its application in advanced electrochemical devices such as batteries and fuel cells. While lithium, sodium, and oxide fast ion conductors have been the subjects of much study, the advent of hydride (H^-) ion fast conductors opens up new windows in the understanding of fast ion conduction due to the fundamental simplicity of the H^- ion consisting of just two electrons and one proton. Here we probe the nature of fast ion conduction in the hydride ion conductor, barium hydride (BaH_2). Unusually for a fast ion conductor, this material has a structure based upon a close-packed hexagonal lattice, with important analogues such as BaF_2 and Li_2S. We elucidate how the structure of the high temperature phase of BaH_2 results in a disordered hydride sublattice. Furthermore, using novel combined quasi-elastic neutron scattering (QENS) and electrochemical impedance spectroscopy (EIS) we show how the high energy ions interact to create a concerted migration that results in macroscopic superionic conductivity via an interstitialcy mechanism.

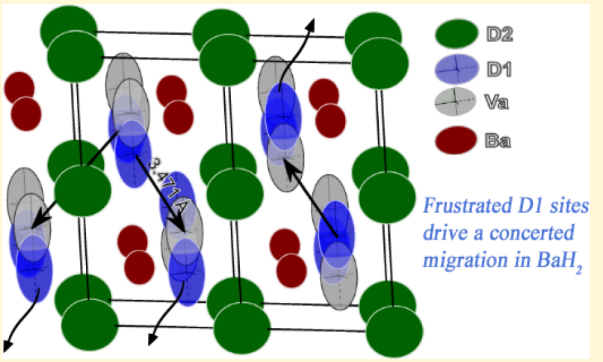

INTRODUCTION

Verbraeken et al. observed high ionic conductivity (>10^{-1} S/cm) at temperatures above 500 °C in BaH_2 demonstrating a new type of superionic conducting solid state material.[1−3] Not only is this conductivity high enough to merit this hydride being classed as a superionic conductor, but the hydride ion can be viewed as the simplest mobile ion that yields fast ion conduction. While a proton, H^+, is simpler, the polarizing power of a proton is so high that it cannot really exist as a free ion in a solid state lattice. The hydride ion, however, is similar in size to other well studied mobile ions such as oxide and fluoride. By studying systems such as barium hydride with its simple H^- anion, researchers can understand what gives rise to superionic conductivity and translate this knowledge to other materials for applications involving more complex ions.

Hydride ion conductors, specifically barium containing materials, have recently come under intense research for their application as cocatalyst for mild-condition ammonia synthesis.[4−7] Results show hydride materials serving as sinks for chemisorbed H-species and thus freeing up transition metal surfaces for further dissociation of N_2 gas.[8] This process fundamentally shifts the rate limiting step away from N_2 dissociation to NH_x synthesis. Further studies have shown that the synthesis of NH_x species occurs on the surface of the hydride materials putting emphasis on the properties of these hydride based cocatalysts, specifically, their ability to transport hydrogen atoms effectively.[9,10] Thus, understanding the relationship between structure and ionic conductivity in a hydride conducting species (such as barium hydride) is of significant practical importance.

Ionic mobility can be studied using electrochemical impedance spectroscopy (EIS) as well as a more specialized technique of quasi-elastic neutron scattering (QENS). Previous researchers have noted the potential utility of a direct comparison between the two techniques.[11,12] Here we report on a combined EIS and QENS in situ study and show how the comparison between the results of the two techniques allows for identification of the diffusive pathway and determination of charge carrier concentration. In addition, we couple these in situ results with analysis of diffraction and total scattering data to show how *geometric frustration*[13] causes dramatic disordering of the high temperature phase of barium hydride, which in turn gives rise to superionic conductivity. Geometric frustration refers to configurational disorder caused by overconstraint—where two competing interactions do not allow for energy minimization (i.e., the creation of an excited state). The classic example of this phenomenon is the Ising

Received: July 4, 2022
Revised: October 24, 2022

triangular antiferromagnet:[13] a system of three magnetic spins placed on an equilateral triangle whose spin can be either +1 or −1 (Ising), and whose energy is minimized when the spins are anti-aligned (+1 next to −1). The assignment of the first two spins is trivial (one +1 and the other −1). However, the third spin will always be *frustrated* as it cannot simultaneously be anti-aligned with both the +1 and −1 spin states.

EXPERIMENTAL SECTION

Pure barium metal was obtained from Sigma-Aldrich and placed inside a glovebox. Approximately 5 g of metal was cut and placed inside a sealed reactor. The reactor was then placed in a tube furnace and heated to 800 °C for 12 h under flowing pure hydrogen/deuterium at 50 cm^3/min (deuterium being used for the samples prepared for neutron powder diffraction). Utmost care was taken to ensure that the sample was not exposed to air or moisture at any stage of the synthesis or experiment (e.g., drying columns, sealed and vac tested containers, and gloveboxes). Once cooled, the reactor was returned to the glovebox and the barium hydride removed from its molybdenum crucible and placed into a mortar and pestle. At this point the material should appear as a dull gray color and maintain its general robustness from before synthesis. The material was ground into a fine powder and placed in a sealed glass vial inside the glovebox. Each batch of BaH_2 was then tested for impurities (namely BaO) via a 1 h XRD scan in which the sample was protected by Kapton Film.

Pure samples were then pressed into 25-mm-diameter pellets with either 3 mm or 1 mm thickness for NPD and QENS, respectively. After sintering at 700 °C for 2 h, the pellets were painted with Pd paste from Gwent to serve as electrodes for the EIS test. Care was taken to place the ∼3-mm-diameter circle electrodes near the edge of the pellet without actually painting the edge (∼1 mm from the edge) in order to keep them out of the neutron beam. The pellets were then placed inside a small furnace inside the glovebox and the electrodes dried at 100 °C for 10 min. Once dry, a special microscope camera connected wirelessly to a computer was used to take close-up shots of the electrodes with a calibrated slide juxtaposed. The images were analyzed via ImageJ, and the average of the two areas per pellet were later used in conductivity calculations (see SI eq 9, A_e). Finally, a caliper was used to measure the thickness near the electrodes (see again SI eq 9, l_e).

After the samples were synthesized, pressed, painted, and the electrodes characterized, they were placed inside a sealed NALGENE bottle and transported to ISIS. Once at ISIS, the samples were loaded into the St Andrews in situ cell inside a glovebox (see Figure S1), with care being taken to ensure good electrical contact between the electrodes and the Mo leads of the cell. The position of the gas and electrical connections were checked and adjusted before the sealed cell was removed from the glovebox and placed inside an RAL 3 or 4 furnace. With the help of the ISIS Pressures and Furnaces Team, the cell was leaked tested, evacuated, and placed inside the Osiris/Polaris diffractometer with the correct orientation for the diffractometer/spectrometer.

Diffraction data for this paper were collected in two experiments on Polaris at ISIS. The first experiment covered the following temperatures: RT, 100 °C, 200 °C, 300 °C, 400 °C, 425 °C, 450 °C, 475 °C, 525 °C, 550 °C, 600 °C, and 650 °C.[14] The data were collected from powder samples in 5% D_2 in Ar. At each temperature, the equivalent of 30 min of data was collected. A different data set was used for 725 °C.[15] This data was collected as part of the total scattering experiment.

Total scattering data were collected on Polaris at ISIS at RT, 400 °C, 600 °C, and 725 °C.[15] Here we focus on the 600 °C data. The data were collected over 4 h and then carefully corrected for multiple scattering, detector inefficiency, furnace, and sample environment related noise. A model was produced using the NPD data refinement results (both 4f and 2d models were produced—see SI) as a starting point. The hexagonal lattice had to first be transformed into an orthogonal cell and then expanded into a supercell of approximately 60^3 $Å^3$ and 12,000 atoms. Bragg data, $S(Q)$, and $D(r)$, were fit concurrently using RMCProfile (Reverse Monte Carlo simulation software[16]). RMCProfile was selected to model the total scattering data as it allows for the simultaneous modeling of local (total scattering data, $S(Q)$, and its Fourier transform, $D(r)$) and global configurations (Bragg data, representing the "average" structure) using "big box" (i.e., supercell, $\sim 10^4$ atoms) simulations. The technique has been previously used to model local disorder in crystalline materials.[17] A vacancy concentration of 17% was applied to the D1 site only to allow for the use of swap command (a fraction, defined by the user, of iteration steps swap two species i and j) without mixing the D1 and D2 sites. The simulations produced on average 2253 moves per atom (less for the 4f assignment—see Table S6).

QENS data were collected on the Osiris spectrometer.[18] For each temperature, the data were grouped into 21 momentum transfer values (one for every two detectors). The spectra were fitted by a model function of a sum of a delta function ($\delta(\omega)$) and one Lorentzian ($L(\omega)$) convoluted with the spectrometer resolution function ($R(Q, \omega)$) and a linear sloping background (see SI). The spectrometer resolution was obtained from a low-temperature measurement of the barium hydride system (200 °C). All data analysis steps have been performed within the Mantid program framework.[19] The Chudley-Elliot model[20] was fit to $\Gamma(Q)$ (the HWHM of $L(Q, \omega)$; see Figure 8a) to obtain residence times and jump lengths. The dip at higher Q is characteristic of long-range diffusion via a single jump length.

RESULTS AND DISCUSSION

Neutron Diffraction Pattern Analysis. We first reconsider the structure of BaH_2, which under ambient conditions is based on a distorted hexagonal close-packed cation Cotunnite ($PbCl_2$) structure (*Pnma*) which transforms at high temperature (>500 °C) to the hexagonal Ni_2In type structure ($P6_3/mmc$). A similar transition from Cotunnite to Ni_2In structure type is also observed in ambient temperature, high pressure studies of both BaH_2 and BaF2,[21] and indeed this pressure driven transition is also observed for the important hcp anion analogues Na_2S[22] and Li_2S.[23] Such transitions to higher symmetry phases under pressure have been previously reported and linked to differing compressibilities within the sublattices.[24] In the high pressure Ni_2In form, the cations have been suggested to occupy the special 2c, 2a, and 2d sites by analogy with BaF_2.[21] Previous studies at high temperature[1] or high pressure[24] on BaD_2 have shown that the D1 atom can be placed on either the 2d or 4f split site.[1,24] We also refined the NPD data using both the 2d and 4f models and found that both returned satisfactory fits. We note here that full refinement of the occupancies, atomic displacement parameters (ADPs, U), and coordinates created unstable fits due to the strong covariances between the three parameters (Figure S2 shows the resulting occupancies from these refinements). Thus, the occupancies were fixed according to the TGA results published by Verbraeken et al. at $x = 1.83$ ($BaH_{1.83}$).[14] With no knowledge of site-specific vacancy concentrations, the vacancies were equally divided between the two hydride sites. Furthermore, for the 4f model, the z-coordinate of the D1 position was fixed according to the refined value given from 550 °C. A comparisons between the fits at 600 °C are shown in Table 1 and Figure 1 (for other temperatures see SI Tables S1−4).

Similar to previously published results, we found that the NPD data refinement was not sufficient to distinguish which site represented the best physical model of the system, as the quality of fits was remarkably similar ($\chi^2 = 1.362$ and 1.384 for 2d and 4f, respectively). The reason for the ambiguity is the

https://doi.org/10.1021/acs.chemmater.2c01995
Chem. Mater. XXXX, XXX, XXX−XXX

Table 1. Refinement Table for BaD_2 at 600 °C Using the 2d and 4f Site Assignments for the D1 Atom[a]

Refinement Parameter	2d	4f
a/b (Å)	4.4498(2)	4.4499(2)
c (Å)	6.6803(5)	6.6805(5)
V (Å^3)	114.558	114.563
Ba$\left(\frac{1}{3}\frac{2}{3}\frac{1}{4}\right)$		
$U_{11} \times 100$	5.09(12)	4.89(12)
$U_{22} \times 100$	5.09(12)	4.89(12)
$U_{33} \times 100$	5.65(18)	5.76(18)
$U_{12} \times 100$	2.55(6)	2.44(6)
$U_{13} = U_{23}$	0	0
D1$\left(\frac{1}{3}\frac{2}{3}z\right)$		
z	(3/4)	0.8151
$U_{11} \times 100$	7.80(23)	7.58(23)
$U_{22} \times 100$	7.80(23)	7.58(23)
$U_{33} \times 100$	47.5(6)	22.7(6)
$U_{12} \times 100$	3.90(11)	3.79(11)
$U_{13} = U_{23}$	0	0
D2 (0 0 0)		
$U_{11} \times 100$	19.07(24)	18.30(21)
$U_{22} \times 100$	19.07(24)	18.30(21)
$U_{33} \times 100$	11.9(4)	13.45(35)
$U_{12} \times 100$	9.53(12)	9.15(11)
$U_{13} = U_{23}$	0	0
χ^2	1.362	1.348
R_p	0.0181	0.0180
R_{wp}	0.0171	0.0170

[a]The occupancy of the D sites was fixed to 0.915 (0.4575) based on the mass loss measured by Verbraeken et al. between room temperature and 725 °C.[14] Errors are shown in parentheses. Other refinement results (temperatures, constrained and full refinement models) are available in the SI Table S1-4.

nature of the phenomenon that is being modeled by the data: high static displacement of the D1 site in the ⟨001⟩ direction. Figure 2 shows the trend in ADPs for the three sites. All three sites show a small jump across the phase boundary; however, the jump in U_{33} for the D1 site is dramatically larger—this is especially clear for the 2d assignment. Note that the 4f split site has approximately half the ADP as the 2d. Verbraeken et al. and Ridley et al. both found that the D1 site showed a relatively large ADP in the HT phase.[1,24] Due to the covariance of U, occupancy, and coordinates, it is possible to find different ADPs. Specifically, Verbraeken et al. proposed a model in which the D2 and Ba sites were significantly distorted from a spherical shape (however, the D1 site remained predominately elongated in ⟨001⟩). A model based on their refinement values is shown in Figure S3.

To understand the rise of the static displacement of the D1 site, first we compare the intersite distances for the 2d and 4f sites (Table 2). By moving in the z-direction from 2d (to the 4f), the D1 atom is able to increase separation from the nearest Ba^{2+} sites from 2.57 Å to 2.62 Å. It can be seen in Figure 3a that if the D1 atoms occupy the 2d site, then the Ba and D ions are coplanar and seem to overlap. Moving the D1 away from this plane relaxes this constraint and stabilizes the HT, hexagonal structure. This movement to the 4f site also decreases the distance between the D1 and D2 positions by 0.24 Å and reduces the distance between D1 and the axially coordinated barium ion to 2.84 Å. Thus, while moving away from the planar Ba atoms, the D1 atom becomes much closer to the electrically repulsive D2 site, as well as the axial Ba sites; this site appears to be geometrically frustrated. This frustration explains the large static displacement observed for both the 2d and 4f site assignments. Figure 3b,c) shows visually the geometry and how it leads to frustration for the D1 site. Figure 3d shows the unit cell given by the 4f refinement.

Total Scattering Studies. To better understand the geometric frustration of the system, total scattering data were collected at 600 °C on Polaris[25] at ISIS and modeled with RMCProfile[16] using 12,000 atoms. RMCProfile simulations require a starting configuration that is then varied using Monte Carlo iterations. The D1 site was modeled using both the 2d and 4f assignments. A spherical distribution was applied to all sites prior to refinement (U_{iso} = 0.05 Å^2). For both assignments, multiple configurations were produced and then averaged to create the partial pair distribution functions ($g(r)$). Additionally, the D1 site was labeled F so that the $g(r)$ for the individual hydride sites could be calculated. A full description of all parameters used in RMCProfile refinements is available in the SI. An example of fitted Bragg and total scattering data for the 2d assignment is shown in Figure 4 (see Figure S5 for the 4f refinement Bragg, $G(r)$, and $S(Q)$ results). In general, the configuration files for the different assignments had similar χ^2 values (see Table S6).

Figure 5 shows the atomic densities from these configurations collapsed into a single cell. The display is an isosurface plot with densities between 50% and 100% the maximum value. The distribution shown by these collapsed supercells matches generally with the structure prediction from the NPD refinement. This is expected as the configuration files were created from the NPD refinement results. However, the distribution of the atoms around their sites started spherically, while the resulting distributions match well with the ADPs given by the NPD refinements. Thus, the results seem to confirm the spherical distributions of the Ba and D2 sites, while the D1 site is more oval. Note, the barium distribution appears larger in this display as it has a higher fraction of atoms in this density range. The relative higher density of the Ba distribution is more apparent when a large range of densities is plotted as a gradient (see Figure S6).

Figure 6a shows the intersite partial pair distribution functions ($g_{ij}(r)$) as modeled by RMCProfile starting with the 2d configuration (a comparison with the 4f results is shown in Figure S7). The results show that the distribution in the first shell $g(r)$ of D1 ions in relation to Ba ions is narrow compared to any other first intersite shell. The width is comparable to the Ba-Ba intrasite shell which corresponds to the unit cell edge. This implies that the D1 sites are highly constrained which seems in contradiction with the site splitting; however, these results are in accord with the geometric frustration which limits movement in the directions perpendicular to ⟨001⟩ and along ⟨001⟩ the D1 site is also constrained by the close approach to the Ba and D2 planes. The peak is centered at 2.64 Å which matches with the NPD fit using the 4f assignment for D1 (2.62 Å) and the 4f model of the total scattering data (2.64 Å, see Figure S7). Since the peak is asymmetrically broadened toward higher values, the 2.64 Å distance represents a minimum approachable distance for the D1 ion to the Ba ion. This result suggests that the 4f assignment is a more representative model of the D1 site and that the D1 atoms do not exist in the positions between the split site (the length would shrink).

https://doi.org/10.1021/acs.chemmater.2c01995
Chem. Mater. XXXX, XXX, XXX−XXX

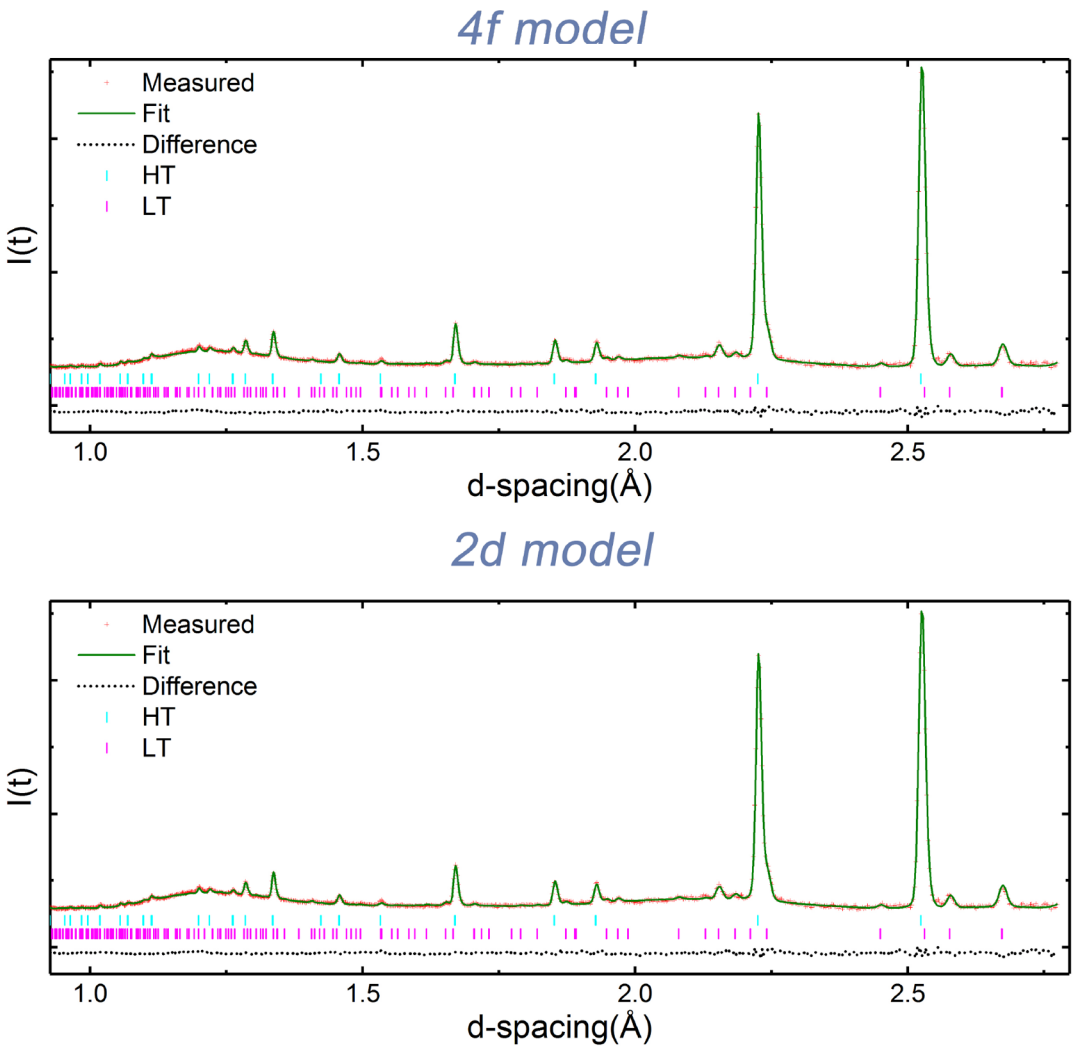

Figure 1. Comparison of Rietveld refinement results for the 4f and 2d assignments for the D1 atom at 600 °C. The two models result in remarkably similar fit results and show that NPD refinement is unable to definitively distinguish between the site assignments. The occupancy for these fits was fixed at 0.875 based off TGA results published by Verbraeken et al.[14] Refinement values for these fits are shown in Table 1, while other refinements are available in the SI.

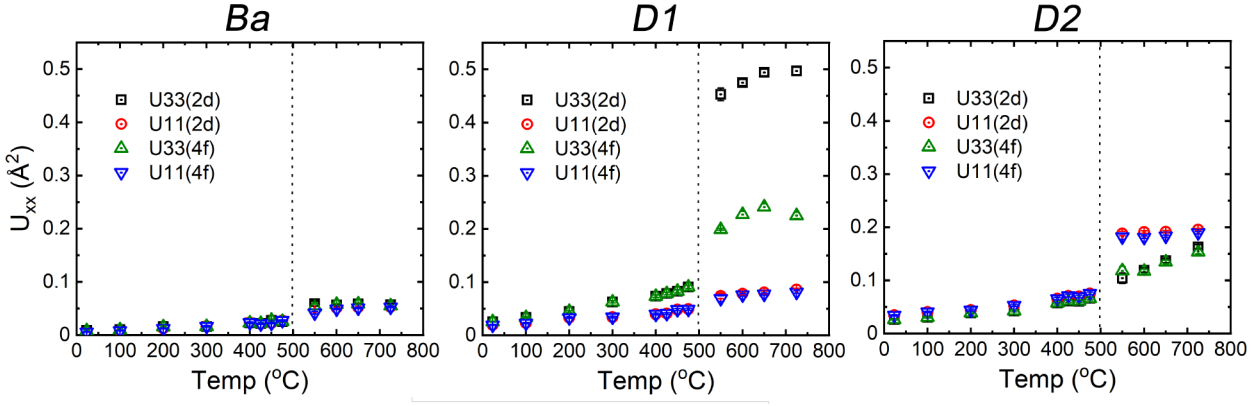

Figure 2. Temperature dependence of ADPs. The Ba site shows a small discontinuation across the phase boundary (dotted line). The D2 site shows a larger jump in its displacement in the $x-y$ plane (U_{11}), while the U_{33} value steadily rises with temperature. However, the jump seen in the D1 U_{33} is dramatically larger than the other two sites. The orthorhombic, *Pnma* coordinates were shifted to match the hexagonal $P6_3/mmc$ structure ($U_{11}^{LT} \rightarrow U_{33}^{HT}$, $U_{11,22}^{LT} \rightarrow U_{11}^{HT}$). Both 4f and 2d assignments predict approximately the same static displacement across the phase transition (note that the 4f split site U_{33} is approximately half the 2d).

Interestingly, the model suggests that the Ba-D2 first shell average distance is significantly shorter than the value predicted by the NPD refinement (2.84 Å vs 3.06 Å). This implies a stronger bond between the D2 and Ba sites, but it

https://doi.org/10.1021/acs.chemmater.2c01995
Chem. Mater. XXXX, XXX, XXX−XXX

Table 2. Table of Important Crystallographic Distances[a]

Bond Length (Å)	4f	2d
Ba-D1 (planar)	2.62	2.57
Ba-D1 (axial)	2.84	3.34
Ba-D2	3.06	3.06
D1-D2	2.82	3.06

[a]The table shows how the assignment of the D1 site affects average distances in the crystal at 600 °C. Importantly, the data shows how moving off the high symmetry 2d site to the 4f site increases the distance between the Ba-center and D1 atom but shortens the length between neighboring D1 and D2 atoms.

also may be related to distortions in the lattice due to the movement of the D1. This movement is reflected in the maximum of the D1-D2 distribution (2.88 Å vs 2.82 Å, for Bragg vs PDF, respectively). The agreement between the Bragg 4f model and the Ba-D1 and D1-D2 $g(r)$ suggests that this site is more likely the better assignment of the D1 atom. Thus, the total scattering data seems to support the idea that geometric frustration is driving the D1 atom away from the 2d site, toward the 4f. The remaining question is the degree to which the three sites are disordered and what that tells us about potential diffusion pathways.

Figure 6b shows pdf results for the intrasite distributions. The D1-D1 first shell has an FWHM that is significantly broader than for D2-D2, consistent with a distribution of D1 sites. The intrasite distance for both Ba and D2 corresponds to distances associated with Bragg scattering, unlike D1. The second peak of these intrasite distributions occur at 4.45 Å in accord with the unit cell edge; however, the D1-D1 peak (4.42 Å) is asymmetrically broadened toward a larger length, reflecting the disorder of D1 in the z-direction. Figure 6c shows that the distances corresponding to this asymmetry are associated with neighboring D1-D1 atoms in the $x-y$ plane. Figure 7a shows a histogram from a 2d configuration of the three sites for the z-coordinate (a comparison with a 4f result is shown in Figure S8). The plot shows that the D1 site is significantly more spread out in ⟨001⟩ than the other two sites. Interestingly, the histogram in the x and y directions (Figure 7b) shows that the sites are generally in agreement with the crystallographic positions, albeit more distributed than predicted by a Gaussian distribution of 0.05 Å^2. Thus, the disordering of the D1 site seems confined to ⟨001⟩ as predicted by the $g(r)_{ij}$.

Angular distribution functions (ADF) were also calculated for each first shell intersite distributions (see Figure 7c). Here, the distributions as predicted by the 4f configuration before refinement have been overlaid as dashed lines. The ADF for D2-Ba-D2 agrees well with the prediction from the NPD refinement results (Bragg). If the D1 atom conformed to the 2d assignment, then we would expect the D2-D1-D2 distribution to look like the D2-Ba-D2 (the 2c and 2d sites are the same Wycoff position, i.e., share the same symmetries).

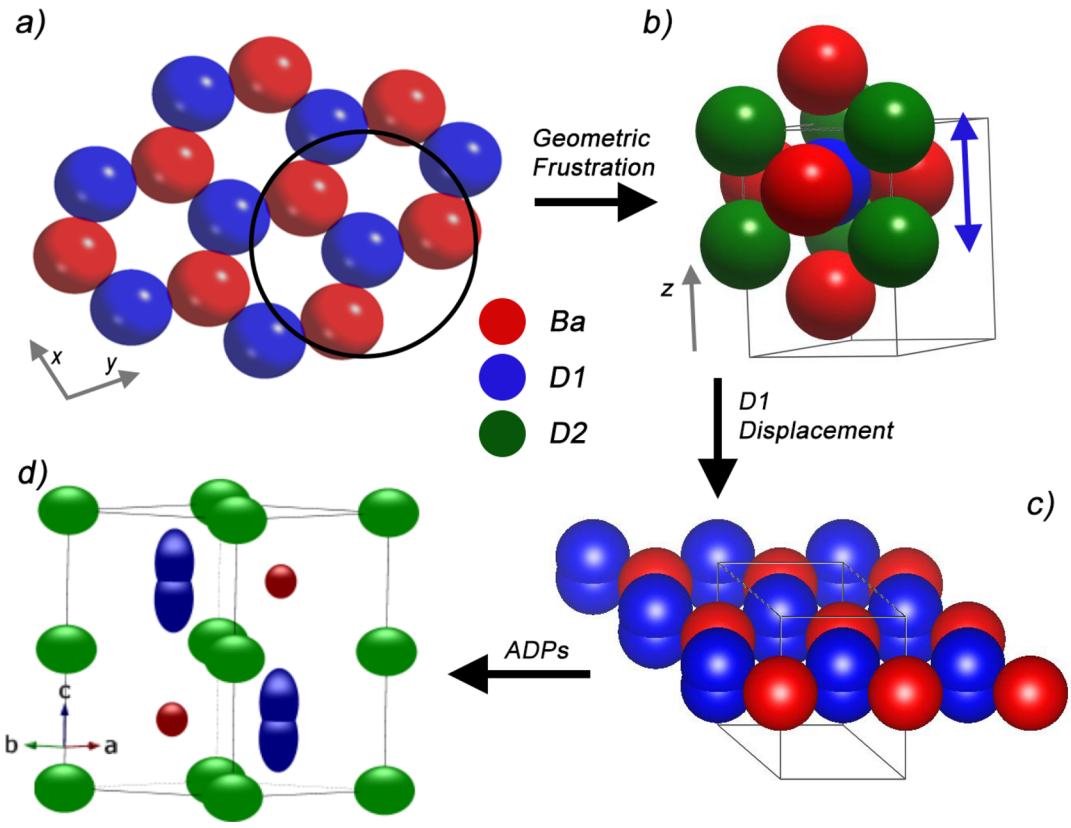

Figure 3. Geometric frustration of the D1 site: (a) Ion arrangement in Ba-D1 plane with D1 at 2d site. The figure shows the spatial arrangement of Ba^{2+} and H^- ions assuming typical ionic radii of 1.34 Å and 1.45 Å respectively. (b) Geometric Frustration of D1 site. This figure shows how the D1 site is caged between the barium sites and the trigonal prism formed by the D2 site; the arrow shows the anticipated tendency for displacement of D1. (c) Ion arrangement of Ba and D1 sublattices with D1 at 4f site. The figure shows the spatial arrangement of Ba^{2+} and H^- ions assuming typical ionic radii; note that D1 sites are at most 50% occupied and that occupation of 1 lobe in real space precludes occupation of the other lobe at the same time. (d) Representation of Refined Structure with D1 on 4f sites. The figure shows ionic positions and refined ADPs at 60% probability.

https://doi.org/10.1021/acs.chemmater.2c01995
Chem. Mater. XXXX, XXX, XXX−XXX

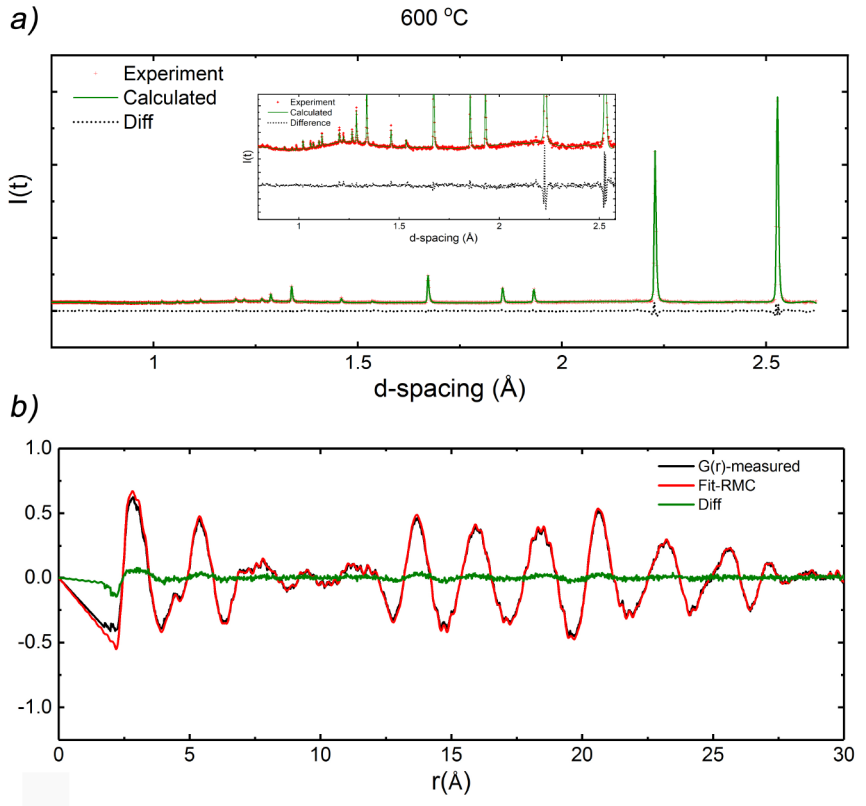

Figure 4. Fit results using RMCProfile for Bragg and total scattering data using the 2d assignment. The fit quality was more-or-less the same for all configuration files (see Table S6). The fit results for the 4f model are shown in Figure S5. The inset shows a zoomed in plot of the background of the diffraction pattern. After subtracting for sources of noise (see Experimental Section), undulations remain, a clear sign of diffuse scattering.

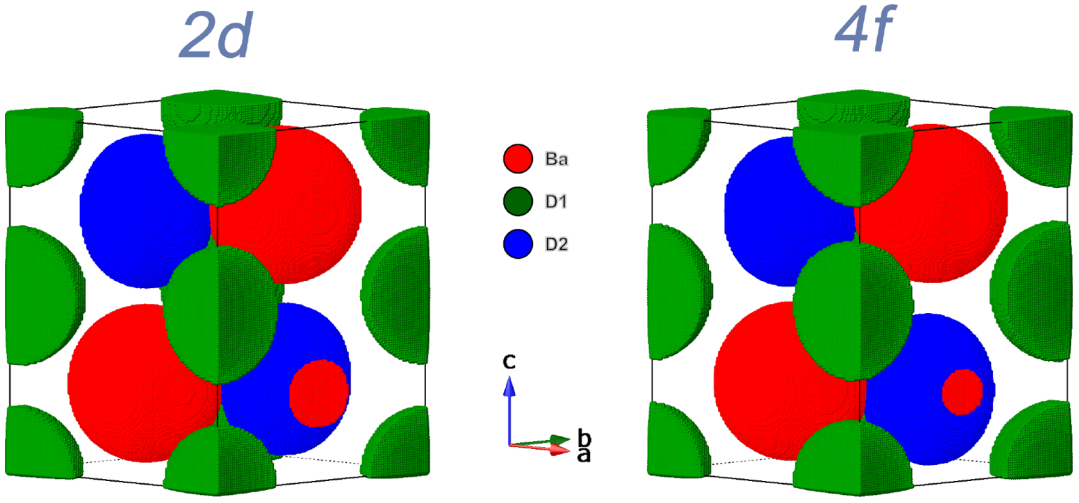

Figure 5. Collapsed supercells from RMCProfile refinement configurations files show a similar average structure to those predicted by NPD refinement (see Figure 3d). The atomic density plots were created from combined density plots for all configuration files. The density plots are isosurface displaying a density between 50% and 100% the maximum value.

The D2-D1-D2 distribution, however, strongly indicates that the 4f site is the better assignment, as the Bragg prediction and the actual ADF are similar. Combined with the D1-Ba-D2 distribution, we can say that in general the D1 atoms appear disordered to a large degree. If the D1 atoms were predominately located at the 4f position, we would expect to see relatively sharp peaks at 80° and 100° in the D1-Ba-D1 distribution.

Together, the total scattering data refinements paint a picture of an ordered structure (Ba and D2 sites) containing a distributed site (D1). Several previously published papers have labeled this phenomenon "liquid-like" or molten sublattices and associated them with high ionic conductivity,[2,26−29] high entropy of phase transitions,[2,27−29] and, more recently, low thermal conductivity.[27] Here, we see that the D1 atom, while disordered, prefers placement on or near the 4f site (see Figures 6b and 7a). The large jump in the ADP of the D1 seen

https://doi.org/10.1021/acs.chemmater.2c01995
Chem. Mater. XXXX, XXX, XXX−XXX

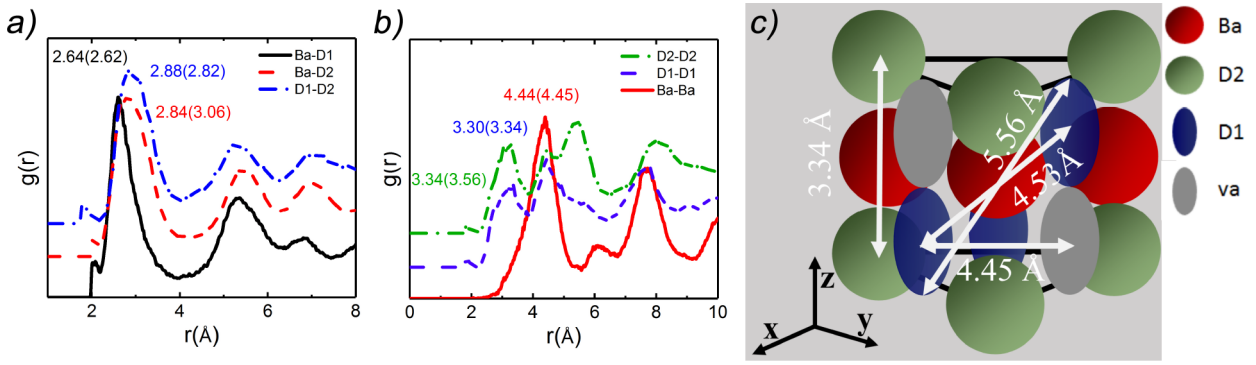

Figure 6. Total Scattering Results: (a) Intersite Pair distribution functions: PDF results from the RMCProfile are plotted with peak maxima *r* values given as well as distances predicted by Rietveld refinement (in parentheses). (b) Intrasite PDFs: The second peak of the D1-D1 intrasite PDF shows an asymmetric broadening toward values >4.45 Å. (c) Intra-D1 atom distances. Considering 4f site as split into two lobes centered on the 2d site, the distance in the basal plane from a lower 4f to one in the next is 4.45 Å, which increases to 4.53 Å for lower to upper. The broadening of the second peak of the D1-D1 intrasite PDF is a result of the distribution of the D1 atoms inside the cavities formed by the D2 and Ba sublattices. This evidenced by the relative broadness of histogram plots in the *z*-direction (see Figure 7).

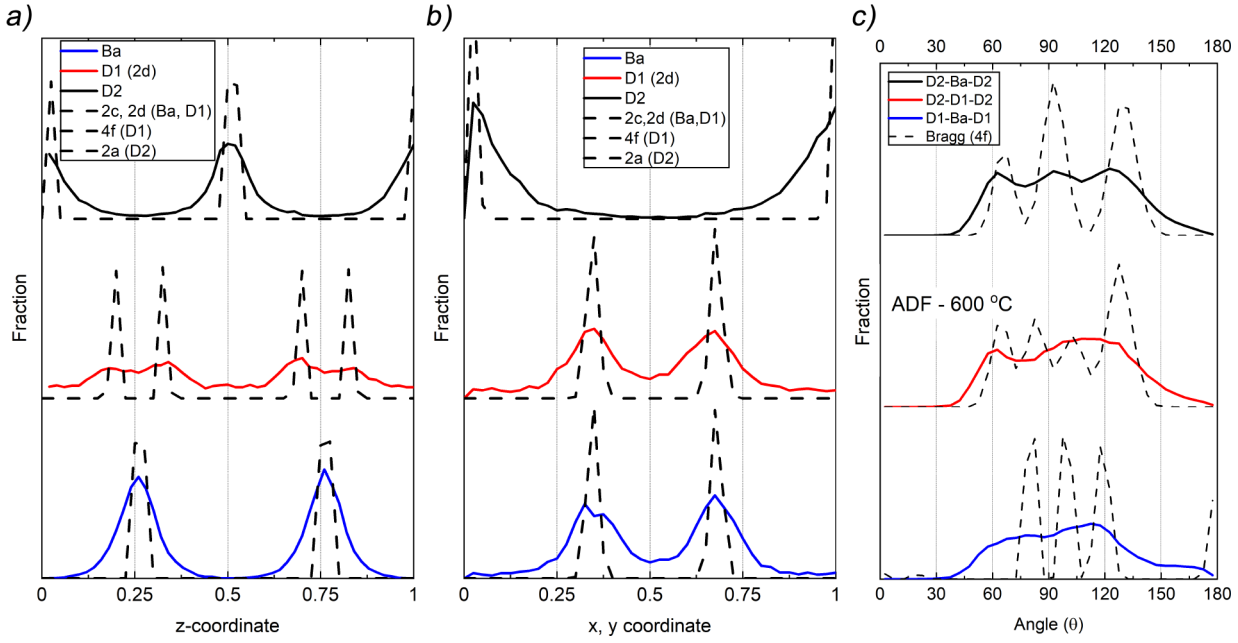

Figure 7. Histograms and angle distribution functions (ADF) produced from the 2d configuration files. The dotted lines are the starting configurations; these have been scaled by 0.5 for ease of comparison for the two histograms. (a) Histogram of the *z*-coordinates for the different sites. The results show the D1 site is significantly more distributed than the D2 and Ba sites. Furthermore, the figure shows that the 2d configuration files result in D1 sites resembling the 4f starting configuration. The D1 site is clearly bimodal; however, a substantial fraction of the atoms remain in the middle of the 4f positions (e.g., the 2d). (b) Histogram of the *x*, *y* coordinates for the different sites. The plot shows that all three sites largely remain centered around their crystallographic sites in the *x*-*y* plane, albiet with a larger distribution than given by a Gaussian distribution of 0.05 Å^2. (c) Angular distribution functions. ADFs are given for the first shell at 600 °C from the RMCProfile refinement (solid lines). The Bragg refinement predicted ADFs are also given (dashed lines). The D2-Ba-D2 ADF shows that in general the D2 and Ba sublattices retain their crystalline order, whereas the D1-Ba-D1 and D2-D1-D2 ADFs show that the D1 site, while being in closer agreement with the 4f assignment than the 2d (e.g., the Bragg ADF for D2-Ba-D2), is highly distributed.

in the NPD data refinement (see Figure 2) suggests a substantial entropic contribution to the energy of the phase transition. This extra entropy is potentially associated with the geometric frustration of the D1 site. With the movement off the 2d site, a large configurational entropy is available to the system in the form of the correlated disorder of the 4f sites (see Simonov and Goodwin for an overview of correlated disorder and configurational entropy[30]). Each D1 atom can either be in an up or down (Ising) configuration, meaning that each Ba-D1 polyhedron has 8 possible configurations associated with it (2^n, compared to 1 for the 2d configuration). The number of configurations grows exponentially with the inclusion of neighboring polyhedron, dramatically increasing the configurational disorder. This could explain the origins of high entropy associated with this class of superionic conductors.

Keen points out that disordered sites that give rise to good ionic conductivity can often be modeled using a single site with large ADPs or as a split site, exactly what we observed from the NPD data.[31] Thus, the D1 site, with its high degree of disordering, seems likely to be a potential reason for the observed superionic conductivity in barium hydride. However,

https://doi.org/10.1021/acs.chemmater.2c01995
Chem. Mater. XXXX, XXX, XXX−XXX

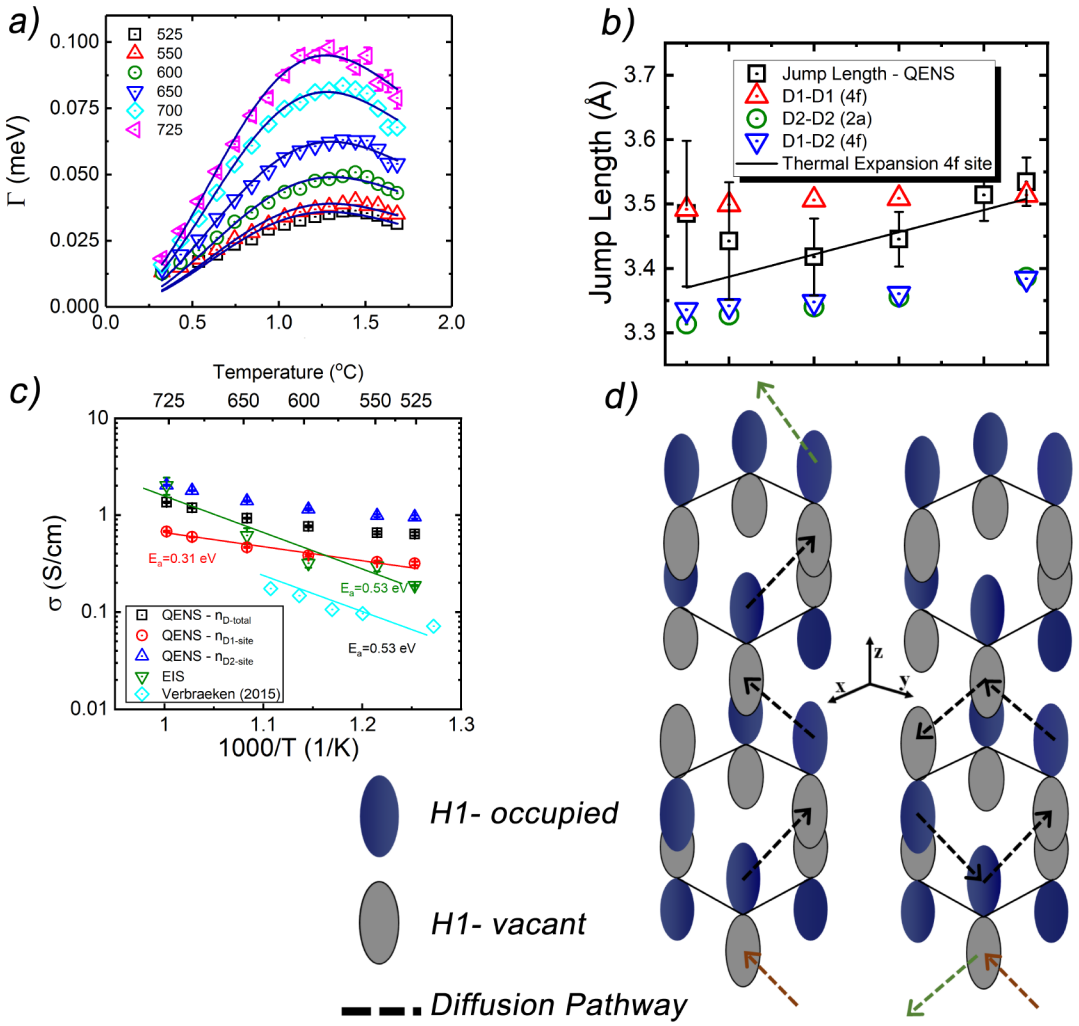

Figure 8. QENS results: (a) Chudley-Elliot Fit. Chudley-Elliot model fit of QENS data collected on OSIRIS spectrometer at ISIS. We see an increase in HWHM (Γ) with temperature, which is to be expected from a diffusive process. The Q-dependence of the broadening observed is characteristic of jump diffusion. (b) Jump Length Comparison. The jump length calculated by fitting the QENS data with the CE model are plotted versus lattice spacings taken from Rietveld fits of NPD data. From analysis of the jump length alone, it is not possible to determine a diffusion pathway as D1 to D1, D2 to D2, and D1 to D2 pathways are all possible. (c) Arrhenius Plot of Conductivity. Comparison between EIS data and QENS result for different pathways and number densities. The conductivity predicted by the QENS data takes into account the dimensionality of the diffusive pathway as well as the charge carrier concentration. Since the two hydride sites have roughly the same number densities, the only difference is the pathway dimensionality which for the given jump length is 3d and 1d for the D1 and D2 pathways, respectively. The comparison to EIS data shows that the D1 pathway gives the closest match between the QENS calculated conductivity and the values measured by the EIS. (d) D1 concerted diffusion pathway. The orange arrow represents the "first mover", while the green is the final jump, and the black are the intermediate jumps. Two pathways are shown.

the presence of the disordered D1 site does not rule out the possibility that the D2 site is involved. Slices taken from the atomic density plots (see Figure S9) show a weak overlapping of the two sites, potentially indicating an intersite diffusion pathway.

To explore potential diffusion pathways further, we now turn to quasi-elastic neutron scattering (QENS) data and the simultaneously collected electrochemical impedance spectroscopy (EIS) data. The techniques are complimentary in that the QENS data allow for direct measurement of local diffusion (jumping), while the EIS data allow direct measurement of system wide (total) conductivity. Assuming no other side modes of electronic conduction, the mechanism that gives rise to local diffusion should produce the total conductivity as measured by EIS.

In Situ QENS and EIS. QENS data were collected on Osiris[32] at ISIS using a modified in situ rig for ultrathin pellets (~1 mm). QENS data sets were collected over 2 h, taking an EIS spectrum every 30 min. The QENS data were fitted using the Chudley-Elliot (CE) jump diffusion model,[20] while the EIS data were modeled using equivalent circuits (see Figures S10 and S11). The two data sets are compared via the Nernst−Einstein equation (see SI eq 5). Figure 8a shows the fit results of the CE model. The Q-dependence of the broadening is characteristic of long-range diffusive motion. The CE model produces a characteristic jump length (l) and residence time (τ) for each data set. Figure 8b shows a comparison between the jump lengths obtained by the CE model and nearest neighbor distances from Rietveld refinement of the NPD data. These data show that the jump lengths are generally closer to the NPD values given by the D1 (4f) configuration; however,

https://doi.org/10.1021/acs.chemmater.2c01995
Chem. Mater. XXXX, XXX, XXX−XXX

because of the closeness of the D2-D2 and D1-D2 distances, it is not possible to identify the pathway from the jump lengths alone. Another study also found the CE model fit the BaH_2 data well.[33] However, their results gave a jump length of 3.1 Å compared with these data values of ~3.45 Å. Interestingly, the authors found no variation in jump length with temperature (over a range of 150 K). Accordingly, the Osiris data was modeled using a fixed jump length of 3.1 Å which returned significantly worse fitting statistics (see SI Table S7). Therefore, analysis went forward using the results shown in Figure 8b.

Einstein diffusion coefficients were calculated for potential pathways. These were then used to calculate conductivity values using the Nernst−Einstein equation and number densities calculated from the NPD data (see SI section in situ QENS). The conductivity values calculated from the QENS data were directly compared with the conductivity values measured simultaneously by the EIS (Figure 8c). These show that by assuming all of the ions are participating in the diffusive motion in 3-dimensions (n_{Dtotal}) we overpredict the conductivity by a factor of approximately 2. The D2-D2 pathway is 1-dimensional and therefore predicts a much higher ionic conductivity than that measured by the EIS. The D1-D1 is 3-dimensional and results in conductivity predictions for the QENS data that match well with the EIS. It is also possible to use a modified Nernst−Einstein equation with an additional term (χ_{vac}) giving the ratio of sites with neighboring sites that are vacant. This model is also unable to reproduce the conductivity values produced from the QENS data modeling (see SI Figures S13 and S14). Therefore, the QENS data seem to indicate a D1-D1 diffusion mechanism. However, there is some disagreement between the EIS data and the QENS model at 525 and 725 °C. At 525 °C, the system exists as a mix of high temperature and low temperature phases resulting in the EIS measured conductivity being some average of the two phases (see Figure S12). At temperatures near the melting point of a superionic conductor a process known as "secondary melting" has been predicted to explain large increases in conductivity.[34] Since BaH_2 decomposes around 750 °C (see Verbraeken et al.[1]), depending upon gas atmosphere, the EIS data at 725 °C could potentially be a result of this type of behavior.

Related to this is the difference in the activation energies of the two techniques, with QENS data returning an E_a of 0.31 eV and EIS data an E_a of 0.52 eV in agreement with Verbraeken et al.[1] Large differences in activation energies are not uncommon as explored by Du et al. and discussed by He et al. in their paper on concerted migration mechanisms.[35,36] In this case the difference arises due to the different timescales of motions being measured by the two probes (EIS and QENS).

EIS measures local vibrations in a system that has a characteristic time scale on the same order as the applied frequency; these could be long- or short-range mechanisms such as vacancy creation or long-range diffusion, while QENS measures displacement of individual atoms over the course of the experiment (several hours). In the case of diffusion in the system, the QENS measured mechanism will be dominated by the dynamics that produce long-range displacement of the atoms. In systems where diffusion takes place by intrinsic vacancy diffusion, the two measurements should have equivalent values. However, in a system where the diffusion does not depend on the formation of the defect first, the two instruments would measure dramatically different values. This type of difference has been noted for molecular dynamics simulations.[35] Interestingly, the E_a value extracted from the QENS data matches well with a range of predicted E_a for a concerted migration mechanism given by He et al. (between 0.2 and 0.4 eV).[36] The mechanism relies on the existence of high energy sites to push out neighboring ions through Coulombic repulsion. They note that high energy sites are typified by elongated spatial occupancies, as observed for the D1 site in the NPD data refinement, and by the broad distribution observed in the z-direction histogram given by the RMCProfile refinement (see Figure 7a).

One possible mechanism that would result in a high energy configuration leading to a concerted migration is a doubly occupied 4f site. For the D1 atoms (approximately randomized in the space defined by a single 4f ADP), the chances a D1 atom has a neighboring vacant 4f site in the next layer to move into is 50%. Since there are three such closest neighbors, the D1 atom on average will have at least one "open" space to move into. When a thermal event causes a first mover to jump to an open site, the movement of the other ion in the twinned site creates a strong Coulombic repulsive force that either causes the first mover to jump back or the other D1 atom to jump to a different 4f site family. This forced jump can set off a cascade effect in which the D1 atoms move into neighboring site to escape doubly occupied 4f sites.The effect of this is the creation of high energy configuration as discussed by He et al. and the overall lowering of the E_a energy associated with long-range diffusion.[36] QENS measurements see this cascade effect and the lower E_a associated with these forced jumps, while the EIS measurements see thermally induced first jumps as well as the concerted migration. A visual representation of this potential pathway for concerted motion is shown in Figure 8d, similar to a mechanism proposed for β-alumina.[37] It is also possible that the first mover is a jump by a D2 atom into a vacant 4f site. However, the inverse is not true, as a D1 jump into a D2 does not result in the necessary high energy configuration that leads to concerted migration and lowering of the E_a.

CONCLUSIONS

Structures of MX_2 arrays based on close packed arrays are well-known as hosts for anion ion conductors, especially cubic close packed cation arrays with the fluorite structure. With larger cations, e.g., Ba, the structure changes to a hexagonal close packed array of the Ni_2In type. For the high temperature form of BaH_2, this MX_2 structure type again shows fast ion transport and here we show this to be facilitated by geometric frustration resulting in a highly disordered high energy site with apparent vacant regions that result in doubly occupied splits sites leading to a concerted migration.

The diffusion pathway resulting in the superionic conductivity of BaH_2 is dominated by D1 to D1 site hoping. NPD results show the D1 site to be highly anisotropically distributed in space formed by the ordered D2 and Ba sublattices. This geometric frustration results in a crystallographic environment in which the ion is unable to reach a low energy state and is statically displaced across a confined space. It has been observed previously that high energy positions in crystals manifest as large anisotropic ADPs.[36] In the case of BaH_2, the D1 site is simultaneously repulsed by the nearby D2 site and barium cation. These forces prevent the D1 ion from reaching an equilibrium state and result in large configurational entropy.

https://doi.org/10.1021/acs.chemmater.2c01995
Chem. Mater. XXXX, XXX, XXX−XXX

This symmetry based disordering is reflected in the large jump in ADPs across the phase transition (see Figure 2).

The distribution along z of the D1 site is further supported by neutron total scattering results that show the D1 atoms to be centered on the 4f sites, while being highly distributed. Combined in situ QENS and EIS results show that the D1-D1 jump pathway is the only mechanism that results in a reasonable match in the data measured by QENS and EIS. This correlates well with the observations made from the diffraction and total scattering data. The fact that the conductivity is predicted well by using the entire number density of the D1 sublattice suggests that the mechanism of diffusion is the result of concerted migration. A concerted migration mechanism is further supported by the apparent difference in activation energy as measured by EIS and QENS, with QENS value falling within the range predicted by He et al. for systems manifesting concerted migration.[36] The driving force behind the rise of superionic conductivity in BaH_2 is the geometric frustration of the D1 site that leads to static disordering across the high temperature phase change and results in a high energy configuration that is susceptible to lower energy barrier diffusive mechanisms.

■ ASSOCIATED CONTENT

Supporting Information

The Supporting Information is available free of charge at https://pubs.acs.org/doi/10.1021/acs.chemmater.2c01995.

2d cif files (ZIP)

4f cif files (ZIP)

Theoretical background, further experimental details, alternative models, and supporting data and figures (PDF)

■ AUTHOR INFORMATION

Corresponding Authors

Gavin J. Irvine − *Department of Chemistry, University of St Andrews, St Andrews, Scotland KY16 9ST;* orcid.org/0000-0001-5823-107X; Email: gji4@st-andrews.ac.uk

John T. S. Irvine − *Department of Chemistry, University of St Andrews, St Andrews, Scotland KY16 9ST;* orcid.org/0000-0002-8394-3359; Phone: +44(0) 1334 463817; Email: jtsi@st-andrews.ac.uk

Authors

Franz Demmel − *STFC ISIS Neutron and Muon Source,, Rutherford Appleton Laboratory, Chilton, Oxon, United Kingdom OX11 0QX*

Helen Y. Playford − *STFC ISIS Neutron and Muon Source,, Rutherford Appleton Laboratory, Chilton, Oxon, United Kingdom OX11 0QX;* orcid.org/0000-0001-5445-8605

George Carins − *Department of Chemistry, University of St Andrews, St Andrews, Scotland KY16 9ST*

Martin Owen Jones − *STFC ISIS Neutron and Muon Source,, Rutherford Appleton Laboratory, Chilton, Oxon, United Kingdom OX11 0QX*

Complete contact information is available at: https://pubs.acs.org/10.1021/acs.chemmater.2c01995

Notes

The authors declare no competing financial interest.

■ ACKNOWLEDGMENTS

I would like to thank the ISIS Facility Development Studentship for funding this work. Additionally, I would like to thank ISIS Neutron and Muon Source for providing the beam time to collect all the scattering data presented in this paper. Finally, I would like to thank the Crockett Scholarship for supporting my studies. For the purpose of open access, the author has applied a Creative Commons Attribution (CC BY) license to any Accepted Author Manuscript version arising.

■ REFERENCES

(1) Verbraeken, M. C.; Cheung, C.; Suard, E.; Irvine, J. T. S. High H ionic conductivity in barium hydride. *Nat. Mater.* **2015**, *14*, 95−100.

(2) Wood, B. C.; Marzari, N. Dynamical structure, bonding, and thermodynamics of the superionic sublattice in α-AgI. *Phys. Rev. Lett.* **2006**, *97*, 1−4.

(3) Myrdal, J. S. G.; Blanchard, D.; Sveinbjörnsson, D.; Vegge, T. Li-ion conduction in the LiBH4:LiI system from density functional theory calculations and quasi-elastic neutron scattering. *Journal of Physical Chemistry C* **2013**, *117*, 9084−9091.

(4) Wang, P.; Chang, F.; Gao, W.; Guo, J.; Wu, G.; He, T.; Chen, P. Breaking scaling relations to achieve low-temperature ammonia synthesis through LiH-mediated nitrogen transfer and hydrogenation. *Nature Chemistry* **2017**, *9*, 64−70.

(5) Gao, W.; Wang, P.; Guo, J.; Chang, F.; He, T.; Wang, Q.; Wu, G.; Chen, P. Barium Hydride-Mediated Nitrogen Transfer and Hydrogenation for Ammonia Synthesis: A Case Study of Cobalt. *ACS Catalysis* **2017**, *7*, 3654−3661.

(6) Hattori, M.; Mori, T.; Arai, T.; Inoue, Y.; Sasase, M.; Tada, T.; Kitano, M.; Yokoyama, T.; Hara, M.; Hosono, H. Enhanced Catalytic Ammonia Synthesis with Transformed BaO. *ACS Catalysis* **2018**, *8*, 10977−10984.

(7) Gao, W.; Guo, J.; Wang, P.; Wang, Q.; Chang, F.; Pei, Q.; Zhang, W.; Liu, L.; Chen, P. Production of ammonia via a chemical looping process based on metal imides as nitrogen carriers. *Nature Energy* **2018**, *3*, 1067−1075.

(8) Kitano, M.; Inoue, Y.; Ishikawa, H.; Yamagata, K.; Nakao, T.; Tada, T.; Matsuishi, S.; Yokoyama, T.; Hara, M.; Hosono, H. Essential role of hydride ion in ruthenium-based ammonia synthesis catalysts. *Chemical Science* **2016**, *7*, 4036−4043.

(9) Abe, H.; Niwa, Y.; Kitano, M.; Inoue, Y.; Sasase, M.; Nakao, T.; Tada, T.; Yokoyama, T.; Hara, M.; Hosono, H. Anchoring Bond between Ru and N Atoms of Ru/Ca 2 NH Catalyst: Crucial for the High Ammonia Synthesis Activity. *Journal of Physical Chemistry C* **2017**, *121*, 20900−20904.

(10) Kitano, M.; Inoue, Y.; Sasase, M.; Kishida, K.; Kobayashi, Y.; Nishiyama, K.; Tada, T.; Kawamura, S.; Yokoyama, T.; Hara, M.; Hosono, H. Self-organized Ruthenium−Barium Core-Shell Nanoparticles on a Mesoporous Calcium Amide Matrix for Efficient Low-Temperature Ammonia Synthesis. *Angewandte Chemie - International Edition* **2018**, *57*, 2648−2652.

(11) Lyonnard, S.; Gebel, G. Neutrons for fuel cell membranes: Structure, sorption and transport properties. *European Physical Journal: Special Topics* **2012**, *213*, 195−211.

(12) Ishikawa, A.; Maekawa, H.; Yamamura, T.; Kawakita, Y.; Shibata, K.; Kawai, M. Proton dynamics of CsH2PO4 studied by quasi-elastic neutron scattering and PFG-NMR. *Solid State Ionics* **2008**, *179*, 2345−2349.

(13) Keen, D. A.; Goodwin, A. L. The crystallography of correlated disorder. *Nature* **2015**, *521*, 303−309.

(14) Verbraeken, M. C.; Carins, G. M.; Irvine, J. T. S.; Owen Jones, M.In situ studies on hydride diffusion and exchange in alkaline earth hydrides by neutron diffraction and thermogravimetric analysis. *STFC ISIS Neutron and Muon Source***2014**.

(15) Irvine, G. J.; Carins, G. M.; Wilson, S.; Irvine, J. T. S.; Owen Jones, M.Combined in situ PDF, NPD and conductivity study of BaD2. *STFC ISIS Neutron and Muon Source***2016**.

(16) Tucker, M.; Dove, M.; Goodwin, A.; Keen, D.; Playford, H.; Slawinski, W. A. RMCProfile User Manual. *Code Version* **2014**, *6*, 0−155.
(17) Tucker, M. G.; Squires, M. P.; Dove, M. T.; Keen, D. A. Dynamic structural disorder in cristobalite: neutron total scattering measurement and reverse Monte Carlo modelling. *Journal of Physics: Condensed Matter* **2001**, *13*, 403.
(18) Irvine, G. J.; Carins, G. M.; Irvine, J. T. S.; Owen Jones, M.QENS studies of conductivity/hydride diffusion in barium hydride. *STFC ISIS Neutron and Muon Source***2017**.
(19) Arnold, O.; Bilheux, J.-C.; Borreguero, J.; Buts, A.; Campbell, S. I.; Chapon, L.; Doucet, M.; Draper, N.; Leal, R. F.; Gigg, M.; et al. Mantid−Data analysis and visualization package for neutron scattering and μ SR experiments. *Nuclear instruments and methods in physics research section a: accelerators, spectrometers, detectors and associated equipment* **2014**, *764*, 156−166.
(20) Chudley, C. T.; Elliott, R. J. Neutron scattering from a liquid on a jump diffusion model. *Proceedings of the Physical Society* **1961**, *77*, 353−361.
(21) Smith, J. S.; Desgreniers, S.; Tse, J. S.; Klug, D. D. High-pressure phase transition observed in barium hydride. *J. Appl. Phys.* **2007**, *102*, 043520.
(22) Vegas, A.; Grzechnik, A.; Syassen, K.; Loa, I.; Hanfland, M.; Jansen, M. Reversible phase transitions in Na2S under pressure: A comparison with the cation array in Na2SO4. *Acta Crystallographica Section B: Structural Science* **2001**, *57*, 151−156.
(23) Barkalov, O. I.; Naumov, P. G.; Felser, C.; Medvedev, S. A. Pressure-induced transition to Ni2In-type phase in lithium sulfide (Li2S). *Solid State Sci.* **2016**, *61*, 220−224.
(24) Ridley, C. J.; Funnell, N. P.; Bull, C. L.; Kohlmann, H. Neutron diffraction study of the α- to β-phase transition in BaD2 under high pressure. *Solid State Commun.* **2020**, *318*, 113965.
(25) Hull, S.; Smith, R. I.; David, W. I.; Hannon, A. C.; Mayers, J.; Cywinski, R. The Polaris powder diffractometer at ISIS. *Physica B: Physics of Condensed Matter* **1992**, *180−181*, 1000−1002.
(26) White, S. L.; Banerjee, P.; Jain, P. K. Liquid-like cationic sublattice in copper selenide clusters. *Nature Communications* **2017**, *8*, 1−11.
(27) Liu, H.; Shi, X.; Xu, F.; Zhang, L.; Zhang, W.; Chen, L.; Li, Q.; Uher, C.; Day, T.; Snyder Jeffrey, G. Copper ion liquid-like thermoelectrics. *Nat. Mater.* **2012**, *11*, 422−425.
(28) O'Keeffe, M.; Hyde, B. G. The solid electrolyte transition and melting in salts. *The Philosophical Magazine: A Journal of Theoretical Experimental and Applied Physics* **1976**, *33*, 219−224.
(29) Boyce, J. B.; Huberman, B. A. Superionic conductors: Transitions, structures dynamics. *Physics Reports* **1979**, *51*, 189−265.
(30) Simonov, A.; Goodwin, A. L. Designing disorder into crystalline materials. *Nature Reviews Chemistry* **2020**, *4*, 657−673.
(31) Keen, D. A. Disordering phenomena in superionic conductors. *J. Phys.: Condens. Matter* **2002**, *14*, R819.
(32) Telling, M. T.; Andersen, K. H. Spectroscopic characteristics of the OSIRIS near-backscattering crystal analyser spectrometer on the ISIS pulsed neutron source. *Phys. Chem. Chem. Phys.* **2005**, *7*, 1255−1261.
(33) Novak, E.; Daemen, L.; Javier, A.; Cuesta, R.; Cheng, Y.; Smith, R.; Egami, T.; Jalarvo, N. Uncovering the hydride ion diffusion pathway in barium hydride via neutron spectroscopy. *Scientific Reports* **2022**, *12*, 1−10.
(34) Maier, J. Crystalline solid electrolytes and defect chemistry: Some novel thermodynamic and kinetic results. *Solid State Ionics* **1996**, *86−88*, 55−67.
(35) Du, Y. A.; Holzwarth, N. A. W. Li Ion Diffusion Mechanisms in the Crystalline Electrolyte γ-Li_3PO_4. *Journal of The Electrochemical Society* **2007**, *154*, A999.
(36) He, X.; Zhu, Y.; Mo, Y. Origin of fast ion diffusion in superionic conductors. *Nature Communications* **2017**, *8*, 1−7.
(37) Wolf, D. On the mechanism of diffusion in sodium beta alumina. *J. Phys. Chem. Solids* **1979**, *40*, 757−773.

https://doi.org/10.1021/acs.chemmater.2c01995
Chem. Mater. XXXX, XXX, XXX−XXX